Envelope analysis applied to non-Hertzian contact simulations in damaged roller bearings

Envelope analysis applied to non-Hertzian contact simulations in damaged roller bearings

Envelope analysis applied to non-Hertzian contact simulations in damaged roller bearings

E Brusa, F Bruzzone, C Delprete, L Di Maggio and C Rosso
Politecnico di Torino, Corso Duca degli Abruzzi 24, Torino,10129, Italy
E-mail: carlo.rosso@polito.it

Abstract. In the latest years many researcher focused on the possibility to foresee the failure of a mechanical system in the early stages in order to allow quick response times. Monitoring and diagnostics are at the base of those methodologies of predictive maintenance, which represents the standard for companies. Data acquired by monitoring systems are sometimes not sufficient to perform an effective diagnosis and to detect failures. In the present work the possibility of a defining a relation between the response of a system and the dimension of a defect causing the vibration is explored. Through a non-Hertzian contact model a roller bearing is studied and a correlation is sought between the size of the defect and the frequency content of the contact pressure time history. Resorting to a non-Hertzian approach enables the determination with good accuracy of the overpressures due to edge effects caused by the sudden change in curvature in presence of a defect. The estimation of the pressure variation can be used to estimate the amplitude of the harmonic content exciting the bearing during operation. Using algorithms for the signal analysis already assessed in the literature, in particular the envelope method, an in-depth analysis of the harmonic content of the signal to consider is possible. The possibility of building a correlation between the load and the size of the defect which might help to identify the dimension of a damage from the estimated frequency content. It is then possible to identify the presence and nature of the defect, allowing an early diagnosis of the failure.

.

1. Introduction

In the recent years, researchers have focused their attention on improving the ability to perform predictive maintenance, also called Condition Based Monitoring (CBM). CBM has huge advantages with respect to classical maintenance in terms of lower costs, less failures and increased up-time of the production lines wich quickly repays the initial investments [1] due to the sensors and acquisition systems required. Also the concept of Remaining Useful Life (RUL) [2] is central to the development of CBM since the construction of health indicators is fundamental to estimate the conditions of machines while in operation. The most common methods to build those indicators are lubricant and vibration analysis, with the second being the most prevalent one since it immediately shows any change in the system and can be paired with powerful signal analysis approaches. Those are able to enhance the eventual presence of faults within mixed signals which convey the information of the multitude of components making up the monitored machines. Using Vibration Based Condition Monitoring (VBCM) vibratory or acoustic signals are analyzed in time, frequency and time-frequency domain [3]. Instead in lubricant analysis a considerable amount of time usually passes between the acquisition of

the sample and its analysis, but online systems have also been developed [4]. Of particular concern is the monitoring of rolling element bearings since their failure can lead to breakdown in the components they support and they also affect the dynamic response and stability of rotating machinery [5] [6]. Early fault detection in those components is then critical to avoid more severe damages in the system but their vibration is the result of various statistically independent components all mixed up in the acquired signal. The separation of the periodic from random components and then of the stationary from non-stationary contributions is done through Blind Source Separation (BSS) [7] [8]. It is well known in literature that due to the random slip in rolling elements the dynamic response of bearing with local defects has to be considered cyclostationary, so with non-deterministic charasteristics, in constrast to the response of components such as gears ([9], [10], [3], [11], in which due to their charasteristics, when order tracking is employed the signal spectrum has discrete frequency components ([12], [13], [14], [15]). Moreover, in rolling bearings with faults, bursts excite high frequency resonances when the rolling element strikes the defect on the inner or outer race, hence the information linked to the ball passing frequencies is not directly available in the raw signal of the vibratory data or its analysis through Fast Fourier Transform (FFT). Envelope analysis overcomes this limitation and was developed with the name of High Frequency Resonance Technique (HFRT) ([16], [17], [18], [19], [20], [21]) and taking advantage of digital filtering using the Hilbert transform [22] can highlight carrier and modulating frequencies in amplitude modulated signals. Indeed the spectra of the demodulated bearing signals shows fault frequencies with sidebands spaced by the shaft rotational frequencies which can also be highlighted with Orthogonal Empirical Mode Decomposition (OEMD) [23]. Regardless of the method, once the frequencies with sidebands are highlighted the position of the fault in the bearing can be located comparing its frequency with the characteristic frequencies of the bearing, namely the Ball Passing Frequency Outer race (BPFO), Ball Passing Frequency Inner race (BPFI) or the Fundamental Train Frequency (FTF) related to the cage speed which are described by the following kinematic relations [4].

$$BPFO = \frac{nf_r}{2}(1 - \frac{d}{D}cos(\phi)) \tag{1}$$

$$BPFI = \frac{nf_r}{2}(1 + \frac{d}{D}cos(\phi)) \tag{2}$$

$$FTF = \frac{f_r}{2}(1 - \frac{d}{D}cos(\phi)) \tag{3}$$

where f_r is the rotational frequency, n the number of rolling elements, ϕ the load angle, d the rolling element diameter and D the distribution diameter. When dealing with signals the choice of the optimal demodulation frequency band is very important and in this context time-frequency analysis is very helpful. Faulty bearings are charachterized by impulsive and time-localized phenomena for which frequency and FFT analysis are not very effective. With limitations, the Short Time Fourier Transform (STFT) or the Wavelet transform are able to localize those harmonic contributions even in time. Both those transform can be used to obtain the Spectral Kurtosis (SK) of the signal [4] as

$$SK(f) = \frac{\langle |X(f,t)|^4 \rangle}{\langle |X(f,t)|^2 \rangle^2} - 2 \tag{4}$$

where $X(f,t)$ is the transform of the signal and time averaging is indicated by $\langle \cdot \rangle$. Frequency bands with the highest Kurtosis are well know to be an indicator of impulsiveness ([24], [25], [26], [27], [28]) and thus the signal content strictly related to impulsiveness are accentuated but also Wavelet denoising ([29], [30], [27]) can be considered an alternative to SK to enhance the bearing signal. Envelope analysis was also shown to be a powerful tool in bearing diagnostic ([31],[32],

[33], [15]), while also data-driven models for CBM have proven to be succesful in this field ([34], [35], [36]). However the link with the analyzed physical phenomena is weaker than envelope-based methods which heavily rely on physical considerations regarding cyclostationarity and amplitude modulation. The present preliminary study aims to contribute to this growing area of research by exploring the possible connection between the health indicators extrapolated from envelope analysis of computed pressure signals and the size of the defect. In particular the harmonic contribution given by the first fault characteristic frequency in the spectrum of the pressure signal is analyzed. The pressure signal is obtained through simulations of the contact between a roller element and a defected inner inner race of a real bearing, whose microgeometrical data has been measured in detail, through the application of a non-Hertzian contact model capable of accurately describing the pressure conditions even with the sudden curvature radii variations typical of defects. The simulated pressure signal is then anlyzed to extrapolate the diagnostic informations using well established techniques generally applied to accelerometric signals experimentally obtained. Indeed, the dynamic response of a system is influenced by the harmonic components of the different subsystems and by different types of excitation sources (gears, misalignment, eccentricities, friction, etc. [37]) as well as noise. Furthermore, in the case of damaged bearings, the impulses caused by the passage of the rolling elements on the localized defect are limited in time and therefore the harmonic content is localized in the high frequency bands. For this reason signal treatment will be applied to the pressure signal to highlight the information on those impulsive phenomena in rolling elements in the high frequency range.

2. Geometry of the bearing

The bearing here analyzed is a FAG 534176, visibile in Fig. 1 which has a static load rating $C_0 = 750\ kN$ and a dynamic load rating $C = 455\ kN$ and 44 cylindrical rollers subdivided in 2 rows. The main dimensions of the bearing are listed in Table 1 in which also the curvatures of the inner race and the roller elements,c_i and c_r are listed. Those curvatures are not usually supplied by the producers but are vital to correctly estimate the pressure distribution and have been obtained by measuring the actual bearing using a Coordinate Measuring Machine (CMM). The measured geometry of the inner race is visible in Fig. 2. Also the load angle is not usually available which for this bearing is $\phi = 12.82°$. Throughout the paper the shaft rotational frequency will be considered constant and equal to $f_r = 15.8\ Hz$ ($\omega_r = \sim 950\ RPM$). Using Eq. 2 at the set rotational frequency results in a $BPFI = 231.9\ Hz$.

Figure 1. FAG 534176 roller bearing.

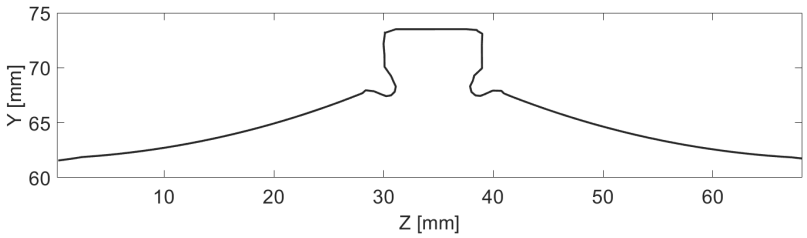

Figure 2. Detailed geometry of the inner race obtained from a CMM.

Table 1. Main bearing dimensions.

Dimension	Symbol	Value [mm]
Inner diameter	d_i	110
Outer diameter	D_o	180
Inner race curvature radius	c_i	83.1
Roller maximum diameter	d_r	17.45
Roller curvature radius	c_r	81.5

3. Non-Hertzian contact model

In order to obtain accurate pressure distributions, even in presence of a defect, a frictionless non-Hertzian numerical 3D surface contact model was used. The contact conditions can be expressed in the so called Hertz-Signorini-Moreau problem ([38], [39], [40])

$$\mathbf{h} \geq \mathbf{0}, \mathbf{p_n} \geq \mathbf{0}, \mathbf{h} \cdot \mathbf{p_n} = \mathbf{0} \tag{5}$$

The first condition enforces that no interpenetration can occur between the contact bodies and therefore the gap function $\mathbf{h}$, which measures the distances between the surfaces, can only be positive, or equal to $\mathbf{0}$ in the contact area. In Eq. 5 and in the following bold lowercase variables represent vectors, while bold uppercase variables represent matrices. The second condition imposes that the contact is non-adhesive and therefore no tension force can be present in the contact area, formulated from the normal stress

$$\boldsymbol{\sigma_n} = \mathbf{t} \cdot \mathbf{n} \tag{6}$$

where $\mathbf{t}$ is the traction force vector and $\mathbf{n}$ is the normal direction to the surface and $\mathbf{p_n} = -\boldsymbol{\sigma_n}$. The third condition enforces that the normal pressures can only be different from $\mathbf{0}$ inside the contact area where $\mathbf{h} = \mathbf{0}$ and null everywhere else. The gap function $\mathbf{h}$ is expressed as

$$\mathbf{h} = h_0 + \mathbf{g} + \boldsymbol{\delta} \tag{7}$$

where h_0 is the indentation between the profiles imposed as a rigid body motion, $\mathbf{g}$ is the initial separation of the contacting surfaces and represents it topography, while $\boldsymbol{\delta}$ represents the elastic deformation of the surfaces due to the applied normal pressure $\mathbf{p_n}$ and can be expressed as [41]

$$\boldsymbol{\delta} = \mathbf{C} \cdot \mathbf{p_n} \tag{8}$$

where $\mathbf{C}$ is a matrix of the influence coefficients which introduces the elasticity of the contacting surfaces. Its components C_{ij} $(i, j = 0, 1, \ldots N)$ relate the displacement δ_i at a point i due to the application of a unit pressure at point j. The pressure distribution is estimated on the triangular grid forming linearly-varying pyramidal pressure elements and the definition of the influence coefficients C_{ij} is detailed in [42] [43] and the solution procedure, which needs two iterative loops, one to eliminate tension forces and one to obtain the correct initial indentation h_0, is described in [44]. The computational model to which this contact algorithm will be applied is visible in Fig. 3 alongside with the representation of the geometry of the defect that will be introduced on the inner race. Throughout the paper the lenght l of the defect will be constant and equal to 500 μm, while the depth h will be varied from 15 μm up to 100 μm, and its width will be $w = 2 \cdot h$. Several force levels will be analyzed, namely $F_1 = C_0 = 750kN$,

$F_2 = \frac{2}{3}C_0 = 500kN$ and $F_3 = \frac{1}{3}C_0 = 250kN$. Examples of the obtained pressure distributions for those force levels and different defect sizes are visible in Fig. 4 in which the non-Hertzian properties of the applied contact model are apparent even for the cases with no defect. Indeed the pattern of the pressure distribution is Hertzian only for the lowest load, while for the other two load cases the edges of the roller come into contact with the inner race, causing overpressures which are predominant for the highest load. Introducing the defect in the middle of the contact area introduces further overpressures, due to the sharp edges of the defect and the lack of material underneath the contact area.

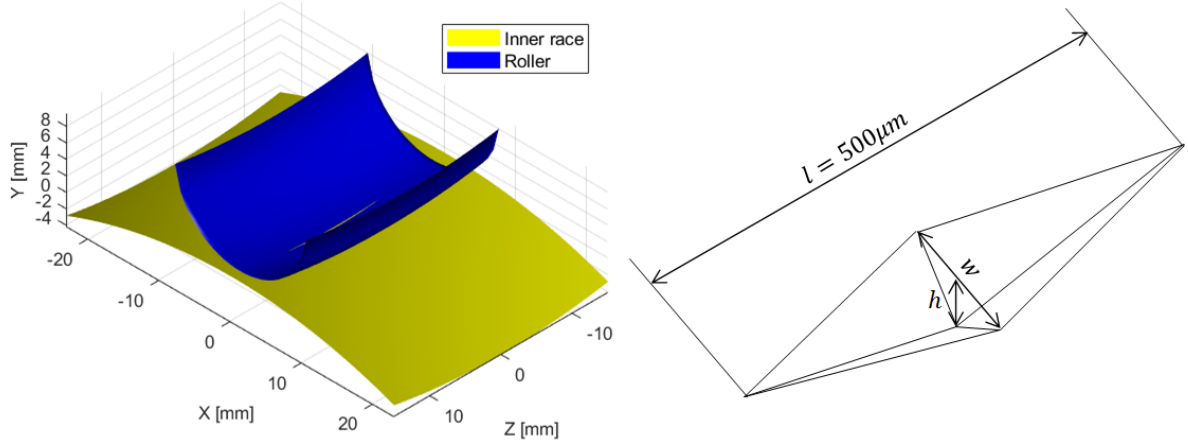

Figure 3. Computational model

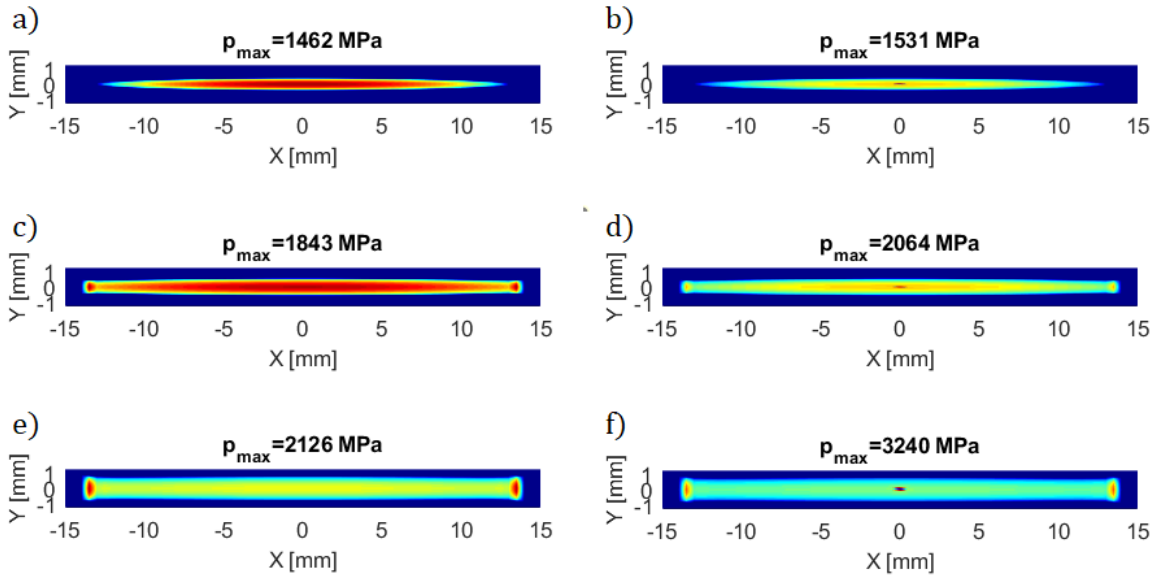

Figure 4. Pressures distributions for different loads and defect size. a) 250 kN, no defect b) 250 kN, 15 μm defect c) 500 kN, no defect d) 500 kN, 50 μm defect e) 750 kN, no defect b) 750 kN, 100 μm defect

4. Results and analysis

The previously described model was used to extract the maximum contact pressure as a function of the rotation angle, numerically simulating around 100 revolutions in order to have a statistically significant sample since the $BPFI$ is not an integer with respect to a single revolution. The obtained time histories for three different load levels and damage dimensions are shown as example in Fig. 5 for the first few revolutions of the inner race. The nonlinear trend of the maximum pressure experienced in the contact zone is depicted in Fig. 6 for all the load cases and defect sizes considered. As an example to show that without further treatment the analysis of this kind of signals yields apparently very little information the FFT of a time history is shown in Fig. 7. Indeed the frequency content of the relevant harmonic of the $BPFI$ is overwhelmed by the amplitude of the lower frequencies and even for this numerically simulated signal no relevant diagnostic information can be immediately extracted. This is expected due to the aforementioned non statistical nature of the signal even though, being numerically generated, its Signal to Noise Ratio (SNR) is extremely high. Regarding experimentally acquired vibration data, the raw spectrum of the acquired signal does not show relevant contributions given by fault harmonics ($xBPFI$). Its shape is modelled in the frequency domain by resonances due to bursts, rather than by fault frequencies. Moreover, operating conditions typical of an industrial context do not exclude a-priori the presence of relevant noise and the manifestation of manifold sources of stationary and non-stationary disturbances. Interestingly, using only the FFT, the trend of the $0Hz$ harmonic contribution for the considered cases results in a seemingly bilinear trend as visible in Fig. 8 even though the maximum pressure, even without defect, follows a nonlinear trend as known in literature [38]. To enhance bearing signal and increase SNR, Fast Kurtogram (FK) and SK were applied as pre-processing steps. The FK of each time history highlighted the optimal frequency bands for the signal demodulation. Furthermore, window lengths to be employed in the STFT for SK computation were selected on the basis of FK (Fig. 9-a). The FK holds a connection between Kurtosis and impulsivity. Using this technique it is possible to highlight the bands where the frequency content has a close correlation to impulsive phenomena. It is even more interesting when applied to experimental signals since it can individuate the informations hidden in the data by non deterministic components, such as noise and structural resonances. In the present work the treatment is applied to a source of excitation rather than what is usually analyzed which is the output of the excitation, the vibration response, obtained through a transfer function essentialy connected to the elasticity of the bodies. Its informative power doesn't properly express in this context since it is not enriched by all other components

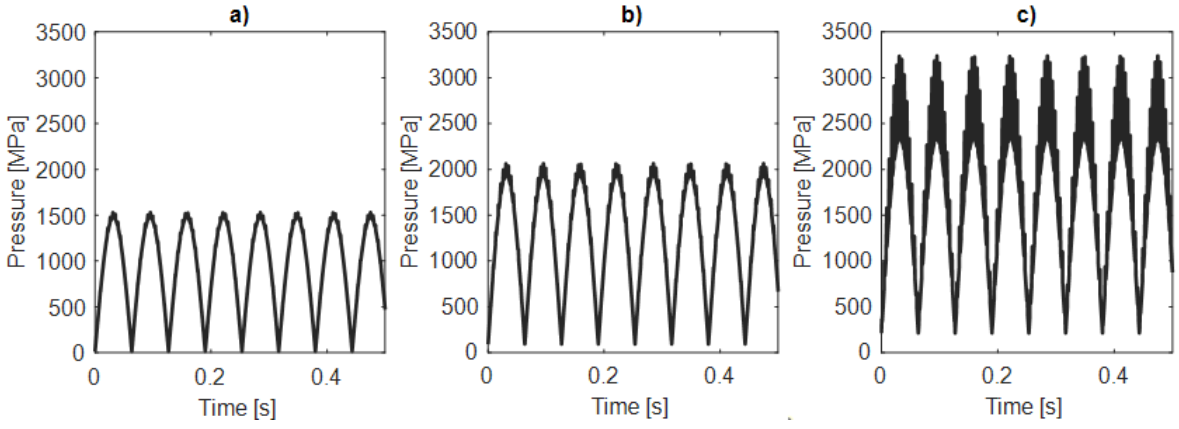

Figure 5. Time histories of the maximum pressure for different cases: a) 250 kN, 15 μm defect, b) 500 kN, 50 μm defect, c) 750 kN, 100 μm defect.

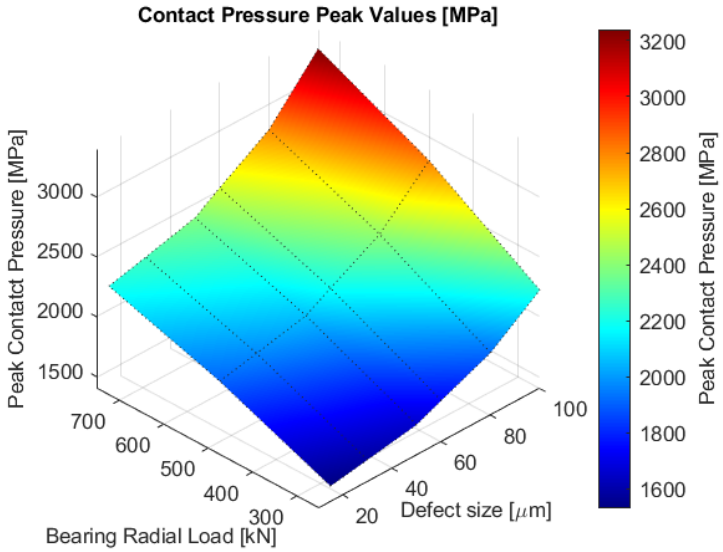

Figure 6. Peak pressures for different loads and defect sizes.

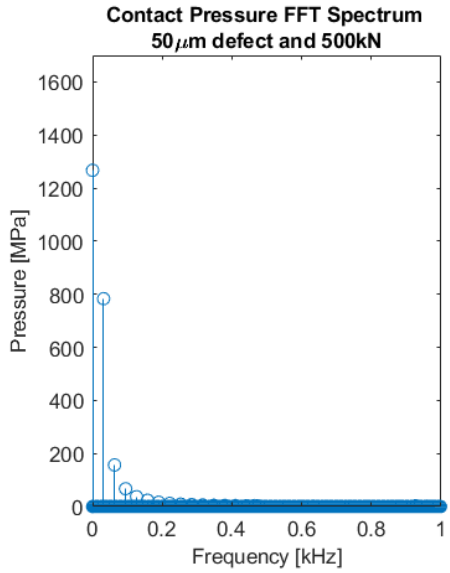

Figure 7. Harmonic content of a time history.

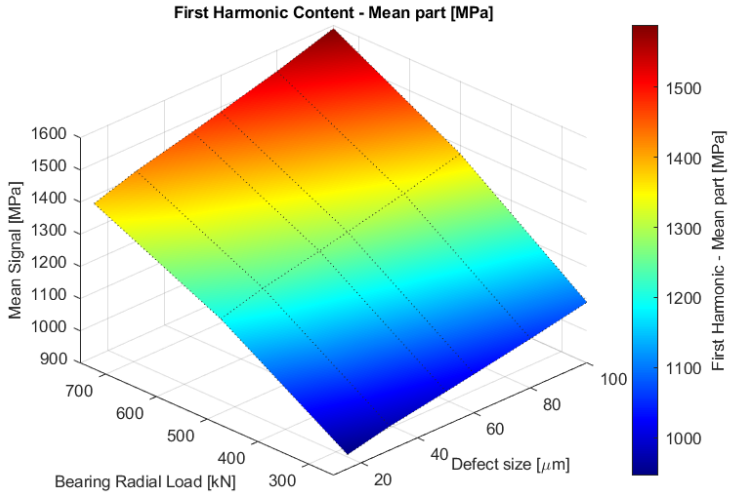

Figure 8. Contribution of the $0Hz$ harmonic at different loads and defect sizes.

usually present in the output signal. Furthermore the impulses simulated through the non-Hertzian contact model are not affected by the damping naturally present in real systems and hence concentrate even more their energy in very short time windows resulting in higher than usual filtering bands with respect to those usually necessary in a real vibration response. The maximum kurtosis criterium was therefore adopted under those considerations to enhance the non-stationary component of the signal, provided that the demodulation bands, thus estimated, were below Nyquist limits. Signal windowing was performed with 80% overlap resulting in the STFT spectrogram of Fig. 9-b. Spectral Kurtosis as a function of frequency before bandpass filtering is shown in Fig. 9-c. For the present case the signal acquisition was simulated equal to

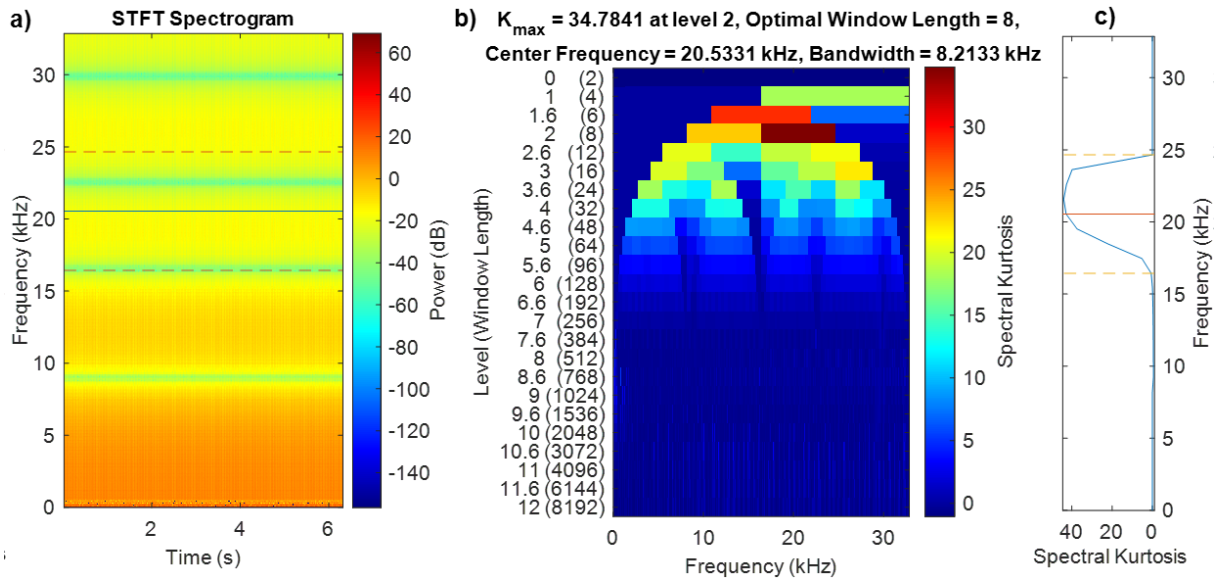

Figure 9. a) Spectrogram of the STFT, b) Kurtogram of the STFT c) Spectral kurtosis of the STFT.

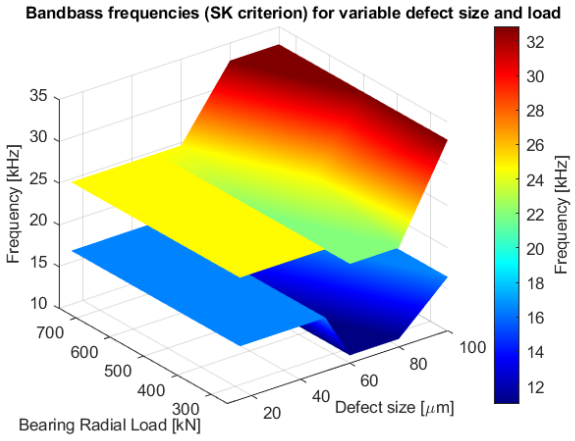

Figure 10. Upper and lower limits of the bandpass frequencies obtained using the maximum Kurtosis criterion.

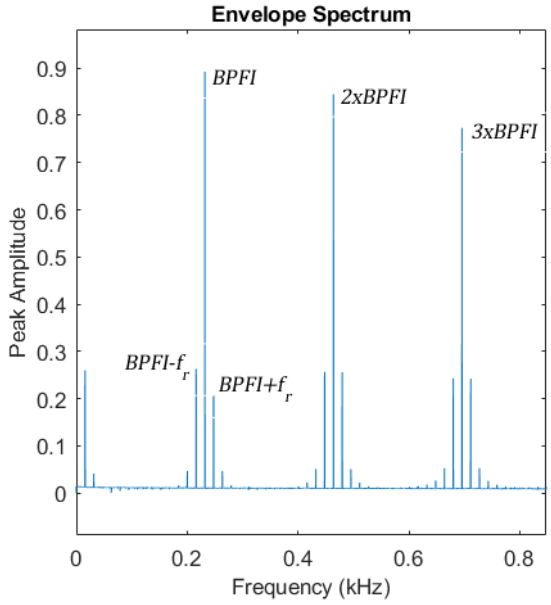

Figure 11. Obtained envelope for the $500kN$ case with $50\mu m$ defect.

$65kHz$, hence setting the Nyquist limit, equal to half of the acquisition frequency, at $32.5kHz$. For the cases with defect size equal to $100\mu m$ and for the case with a $80\mu m$ defect under $750kN$ load the application of the maximum kurtosis criterion suggested an upper bandpass frequency exceeding this limit, hence for those cases the demodulation bands were reduced to avoid aliasing. The upper and lower limits of the bandpass resulting in the application of this criterion for all load cases are visible in Fig. 10. After this steps were preformed, which can be considered as a pre-processing part, the Hilbert transform was computed to demodulate the signal. Hilbert

transformation $\tilde{x}(t)$ of the time signal $x(t)$ is defined as [4]

$$\tilde{x}(t) = \frac{1}{\pi} \int_{+\infty}^{-\infty} x(\tau) \frac{1}{t-\tau} d\tau \tag{9}$$

Basically, it corresponds to a convolution which, in the frequency domain, acquires the form:

$$\tilde{X}(f) = X(f)(-j \cdot sgn(f)) \tag{10}$$

where sgn is the sign function, and j the imaginary unit.This is equivalent to apply FFT to the signal and shifting the phase of positive frequency contributes by $-\frac{\pi}{2}$ and of negative frequency contributes by $+\frac{\pi}{2}$. Practically, the amplitude demodulation with Hilbert transform can be achieved by computing the modulus of the analytic signal. This term refers to the complex time domain signal whose imaginary part is the Hilbert transform of the signal. The real part is represented by the original signal. The modulus of the analytic signal is finally the extracted envelope. The resulting envelope spectrum for the $500kN$ case with $50\mu m$ defect is visible in Fig. 11. As expected now the contribution of the $BPFI$ harmonics is now highlighted and predominant and it shows the typical sidebands, equally spaced by integer multiples of the inner race rotational frequency f_r, emphasizing carrier and modulating frequencies for the different defect sizes. The behavior of the $1xBPFI$ harmonic of the simulated pressure signal is visbile in Fig. 12.

Indeed a trend, altough nonlinear, is noticeable and it's increasing as the load applied and the characteristic dimension of the defect increase. Unexpectedly however, the maximum harmonic content is found for the $80\mu m$ and $250kN$ case which is misleading and similar trend are observed for the higher harmonics $xBPFI$. Indeed this is due to the different bandpass frequencies employed to treat the different simulated signals. Altough no relevant information was immediately apparent in Fig. 7 some information was present. The harmonic contribution

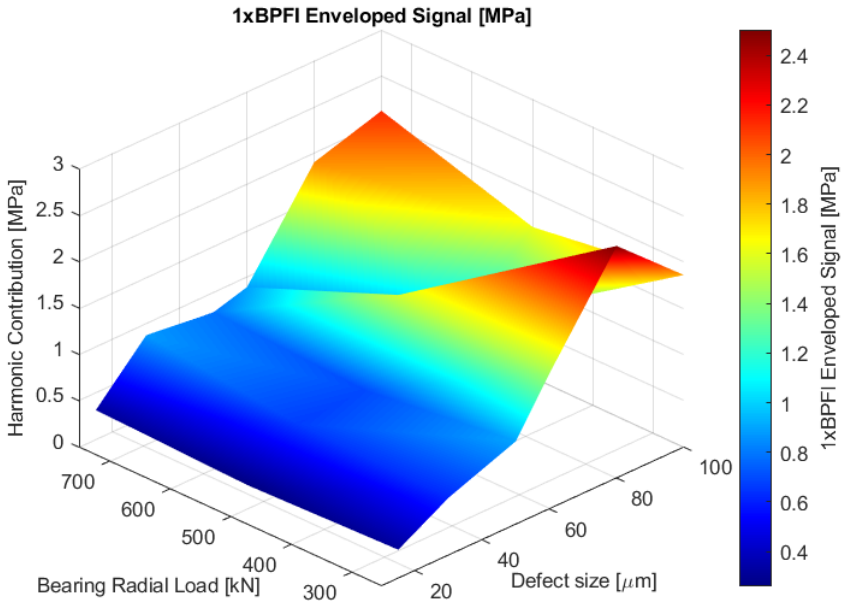

Figure 12. Contribution of the first $BPFI$ harmonic at different loads and defect sizes of the signal envelopes.

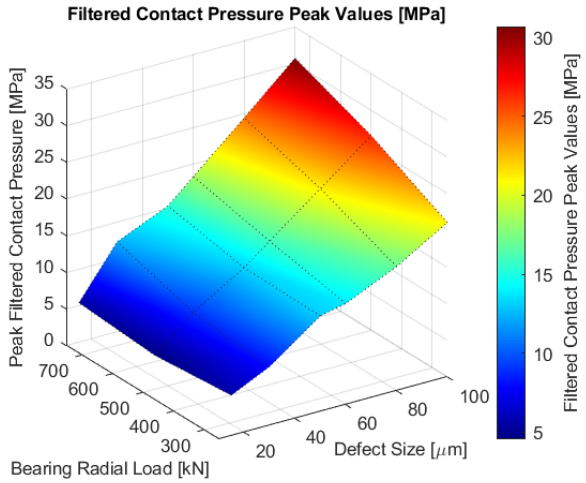

Figure 13. Filtered contact pressure peak values for fixed bandpass frequencies.

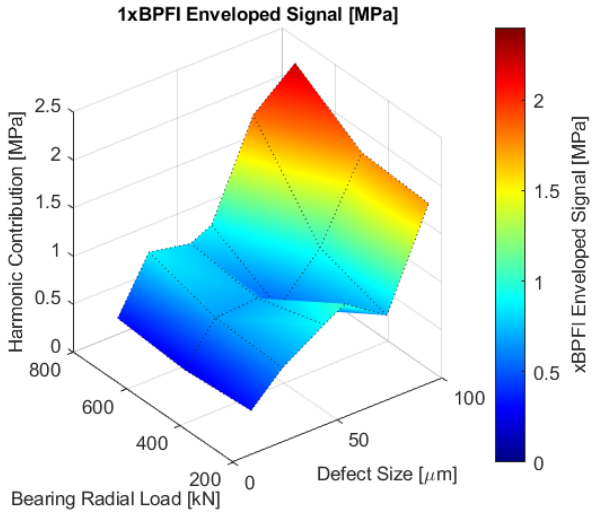

Figure 14. Contribution of the first $BPFI$ harmonic at different loads and defect sizes of the signal envelopes for fixed bandpass frequencies.

of the first harmonic of the shaft rotational frequency f_r obtained directly from the FFT of the raw signal is visible in Fig. 15 which shows a direct dependency to the applied load, while being insensitive to the defect. Instead in Fig. 16 the first harmonic of the $BPFI$ of the FFT of the unmodulated signal has a relationship with both the load and the size of the defect. However, analyzing the FFT of the raw signal is only possible in this case since the signal has been obtained numerically and is untouched by external noise and is also unaffected by the transfer function due to the elasticity of the bodies involved which would result in the measurable vibration. To study the dependency between the modulation bandwith and the results the bandwith to filter the signals has been fixed for all the different cases. The chosen bandwith corresponds to the flat region visible in Fig. 10 for defect sizes from $15\mu m$ up to $50\mu m$ and the resulting contact pressure peak values of the filtered signals is visible in Fig. 13 which show a more direct correletion between applied load and defect size. Similarly the $1xBPFI$ contribution of the enveloped signals using the fixed bandwith is visible in 14 which in this case doesn't convey the misleading information as seen before, but still understimates the harmonic contribution of the $60\mu m$ cases, which show lower content with respect to their neighbouring points. Similar results are obtained if the chosen bandwith is in the range $\frac{f_s}{4}$ and $\frac{3}{8}f_s$, which is a common choice in signal analysis. Arbitrarily choosing instead the fixed bandwith in the range $3xBPFI - 6xBPFI$ $(695.7 - 1391.4Hz)$ yields the harmonic contributions for the first and second $xBPFI$ harmonics visible in Fig. 17 and Fig. 18 respectively. Using this bandpass the $1xBPFI$ shows no correlation with the defect size, but is linearly related to the applied load. Instead the $2xBPFI$ shows a distinctly nonlinear trend in which a correlation between the load and the defect size is evident. Moving to an upper range, specifically $10xBPFI - 13xBPFI$ $(2910 - 3015Hz)$, yields a similar correlation, but this time also for the $1xBPFI$ as visible in Fig. 19, while the $2xBPFI$ contribution, visible in Fig. 20, retains the same trend but with higher values. Indeed, due to the impulsive nature of the overpressure caused by the defect, most of the energy content is located in the higher frequency portion of the spectrum and hence filtering at higher frequency enhances the value of the harmonic content.

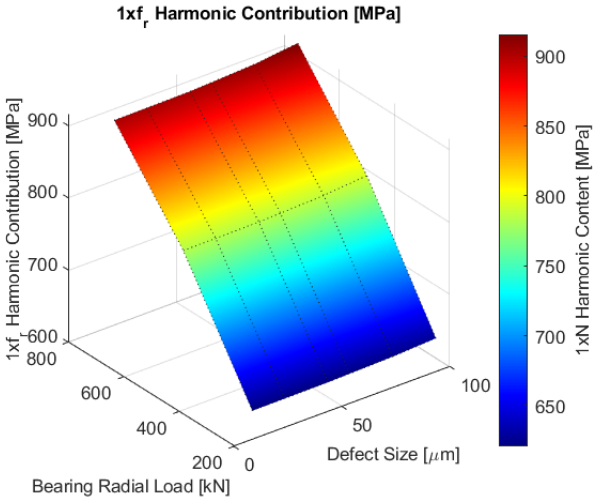

Figure 15. Contribution of the first f_r harmonic at different loads and defect sizes of the raw signal.

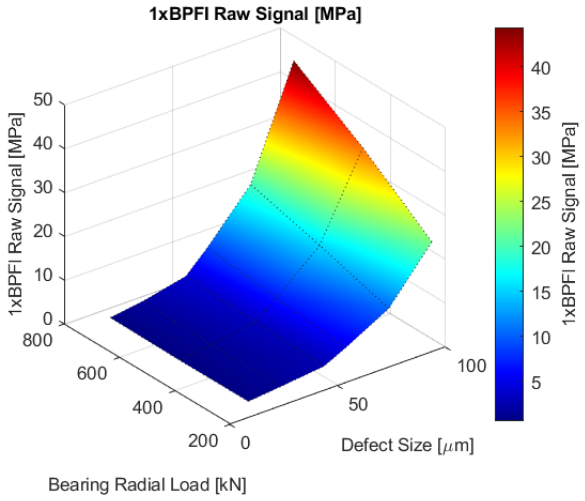

Figure 16. Contribution of the first $BPFI$ harmonic at different loads and defect sizes of the raw signal.

5. Conclusions

In this paper the simulated pressure signal of a roller contacting with a defected inner race has been obtained through a non-Hertzian contact model and then analyzed with well established signal treatment methods to study the harmonic contributions at different pecularіar frequencies seeking a possible correlation between the load and defect size for diagnostic purposes. In a real system the signal analyzed in the present paper is actually the source of excitation which then results in an output vibration dependent on the transfer function due to the nature of the different components of the system. However, it has been shown that only applying

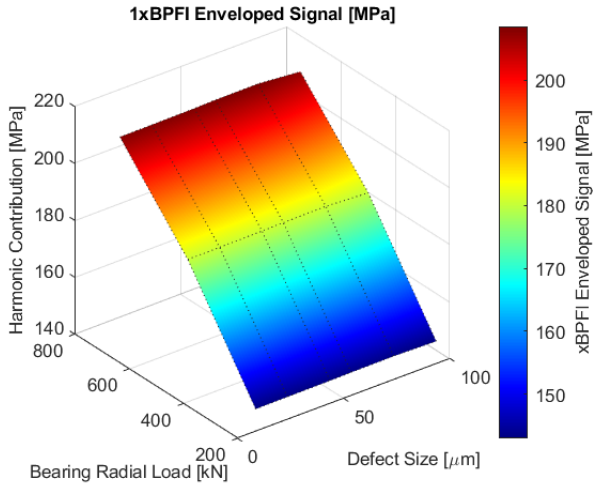

Figure 17. Contribution of the first $BPFI$ harmonic at different loads and defect sizes of the signal envelopes for $3xBPFI - 6xBPFI$ bandpass frequencies.

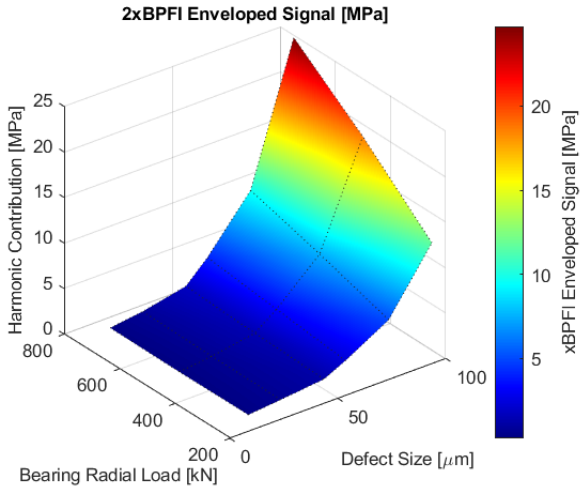

Figure 18. Contribution of the second $BPFI$ harmonic at different loads and defect sizes of the signal envelopes for $3xBPFI - 6xBPFI$ bandpass frequencies.

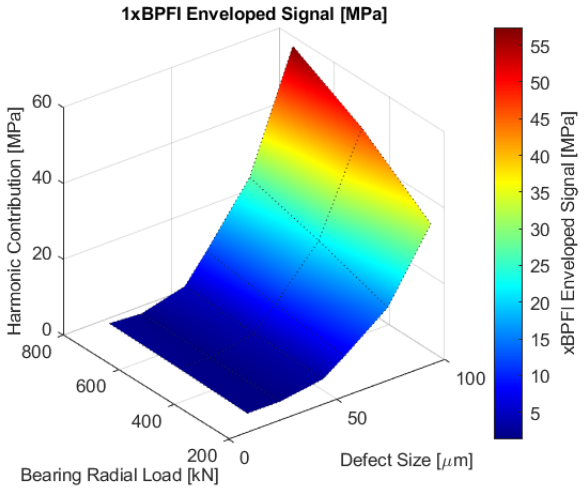

Figure 19. Contribution of the first $BPFI$ harmonic at different loads and defect sizes of the signal envelopes for $10xBPFI - 13xBPFI$ bandpass frequencies.

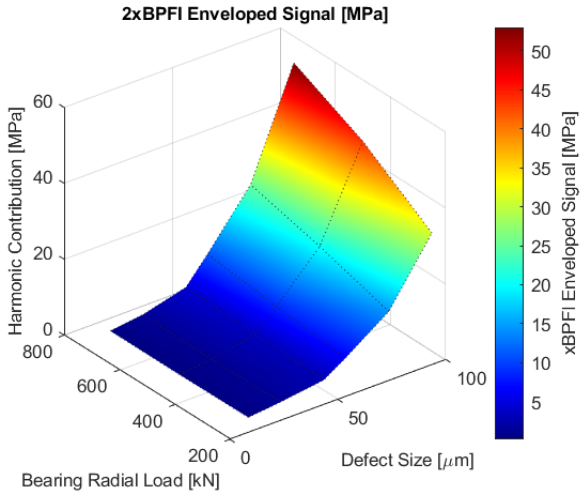

Figure 20. Contribution of the second $BPFI$ harmonic at different loads and defect sizes of the signal envelopes for $10xBPFI - 13xBPFI$ bandpass frequencies.

simple treatments, such as the FFT, yields no valuable information regarding the nature of the defect since those are linearly related only to the load. Instead, when the signal is filtered and demodulated the diagnostic information shows a trend which doesn't have an immediate comparability to the known defect size and loads applied but still some relevant insight is gained. The main parameter influencing the results has been shown to be the demodulation frequency band chosen to treat the signal which affects both the trend and the values of the harmonic contribution. The outputs for several bands were shown and it was observed that filtering in the high range of the $xBPFI$ harmonics yields a trend capable of correlating the harmonic, the load and the defect size indicating a strong diagnostic correlation contained in the numerically obtained signal with the filtering band chosen. It must also be said that the application of digital filtering, such as bandpass and Hilbert transform, in this numerically obtained signal poses the risk of deleting part of that diagnostic content which is evident due to the cleanliess of the signal, its deterministic nature and the absence of other signals capabale of modifying its frequency content. Further studies will be carried out on the subject to deepen the understanding of the diagnostic correlation using the developed methods applied to real vibration data.

References

[1] Mohanty A R 2014 *Machinery condition monitoring: Principles and practices* (Boca Raton, FL, United States: CRC Press)
[2] Wang D, Tsui K L and Miao Q 2018 *IEEE Access* **6** 665–676
[3] Randall R B and Antoni J 2011 *Mechanical Systems and Signal Processing* **25** 485–520
[4] Randall R B 2011 *Vibration-based condition monitoring: industrial, aerospace and automotive applications* (Hoboken, NJ, United States: Jhon Wiley & Sons)
[5] Genta G 2007 *Dynamics of rotating systems* (Berlin, Germany: Springer Science & Business Media)
[6] Genta G, Delprete C and Brusa E 1999 *Journal of Sound and Vibration* **227** 611–645
[7] Antoni J 2005 *Mechanical Systems and Signal Processing* **19** 1166–1180
[8] Antoni J and Braun S 2007 *Mechanical Systems and Signal Processing* **19** Special Issue
[9] McCormick A C and Nandi A K 1998 *Mechanical Systems and Signal Processing* **12** 225–242
[10] Randall R B, Antoni J and Chobsaard S 2001 *Mechanical Systems and Signal Processing* **15** 945–962
[11] Mauricio A, Smith W, Randall R B, Antoni J and Gryllias K 2018 *Proceedings of ISMA 2018 - International*

Conference on Noise and Vibration Engineering and USD 2018 - International Conference on Uncertainty in Structural Dynamics 905–918
[12] McFadden P D 1989 *Mechanical Systems and Signal Processing* **3** 87–97
[13] Potter R and Gribler M 1989 *SAE Technical Paper* 891131
[14] Bonnardot F and Randall R B 2004 *International Journal of Acoustics and Vibration* **9** 51–60
[15] Guo Y, Liu T W, Na J and Fung R F 2012 *Journal of Sound and Vibration* **331** 5644–5654
[16] Burchill R F 1973 *National Bureau of Standards NBSIR* 73–252
[17] Burchill R F, Jhon L F and Wilson D S 1973 *SAE Technical Paper* 730930
[18] Darlow M and Badgley R H 1975 *SAE Technical Paper* 750209
[19] Harting D R 1978 *ISAT* **17** 35–40
[20] McFadden P D and Smith J D 1984 *Journal of Sound and Vibration* **96** 69–82
[21] McFadden P D and Smith J D 1984 *Tribology International* **17** 3–10
[22] Bendat J S 1991 *The Hilbert transform and applications to correlation measurements* (Naerum, Denmark: Bruel&Kjaer)
[23] Delprete C, Brusa E, Rosso C and Bruzzone F 2020 *Shock and Vibration* **8761278** 1–9
[24] Antoni J and Randall R B 2006 *Mechanical Systems and Signal Processing* **20** 282–307
[25] Antoni J 2006 *Mechanical Systems and Signal Processing* **20** 308–331
[26] Antoni J 2007 *Mechanical Systems and Signal Processing* **21** 108–124
[27] Wang D, Tse P W and Tsui K L 2013 *Mechanical Systems and Signal Processing* **35** 176–199
[28] Borghesani P, Pennacchi P and Chatteron S 2014 *Mechanical Systems and Signal Processing* **43** 25–43
[29] Donoho D L and Jhonstone J M 1994 *Biometrika* **81** 425–455
[30] Qiu H, Lee J, Lin J and Yu G 2006 *Journal of Sound and Vibration* **289** 1066–1090
[31] Rubini R and Meneghetti U 2001 *Mechanical Systems and Signal Processing* **15** 287–302
[32] Delprete C, Milanesio M and Rosso C 2005 *Applied Mechanics and Materials* **3-4** 293–302
[33] Sawalhi N and Randall R B 2001 *Non Destructive Testing Australia* **45** 59
[34] Tabrizi A, Garibaldi L, Fasana A and Marchesiello S 2015 *Meccanica* **50** 865–874
[35] Herp J, Ramezani M H, Bach-Andersen M, Pedersen N L and Nadimi E S 1978 *Renewable Energy* **116** 164–172
[36] Pinheiro A A, Brandao I M and Da Costa C 2019 *European Journal of Engineering Research and Science* **4** 12–16
[37] Bruzzone F and Rosso C 2020 *Machines* **8** 37
[38] Jhonson K L 1985 *Contact Mechanics* (Cambridge, United Kingdom: Cambridge University Press)
[39] Kalker J J 1990 *Three-Dimensional Elastic Bodies in Rolling Contact* (Berlin, Germany: Springer)
[40] Wriggers P 2002 *Computational contact mechanics* (Berlin, Germany: Springer)
[41] Sayles R S 1996 *Tribology International* **29** 639–650
[42] Kalker J J and Van Randen Y 1972 *Journal of Engineering Mathematics* **6** 193–206
[43] Boedo S 2013 *Tribology International* **60** 116–118
[44] Marmo F, Toraldo F, Rosati A and Rosati L 2018 *Tribology International* **53** 1415–1440